# Understanding droplet collision with superhydrophobic-hydrophobic–hydrophilic hybrid surfaces

Freshteh Sotoudeh[1], Reza Kamali[1], Seyed Mahmood Mousavi[1*], Nader Karimi[2,3], Bok Jik Lee[4], Danial Khojasteh[5]

[1] *School of Mechanical Engineering, Shiraz University, Shiraz, 71936-16548, Iran*

[2] *James Watt School of Engineering, University of Glasgow, Glasgow, G12 8QQ, United Kingdom*

[3] *School of Engineering and Materials Science, Queen Mary University of London, London, E1 4NS, United Kingdom*

[4]*Institute of Advanced Aerospace Technology, Seoul National University, Seoul 08826, Korea*

[5]*Water Research Laboratory, School of Civil and Environmental Engineering, UNSW Sydney, NSW, Australia*

**Abstract**

This study uses a two-phase finite volume method to investigate the dynamics of Newtonian and non-Newtonian droplets impacting onto hybrid surfaces with various wettabilities. Six configurations with different substrate contact angles are tested ranging from hydrophilic, hydrophobic, and superhydrophilic as well as a combination of them. The temperature-dependent properties are applied to model the Newtonian droplets, and the Arrhenius law which is a relation between viscosity and shear rate is incorporated for the non-Newtonian rheology. The results show that for a hybrid surface with the linear wettabilities varying from hydrophilic to hydrophobic to superhydrophobic, the maximum spreading factor is larger for both Newtonian and non-Newtonian droplets in comparison to any other surface configurations considered in this study.

[*] Corresponding author; Email address: sm.mousavi@shirazu.ac.ir

However, this spreading factor is minimum when a stepwise superhydrophobic-hydrophobic-hydrophilic hybrid surface is examined. Further, the residence time of Newtonian droplet has the maximum value when collides upon a hybrid surface with linear wettability distribution ranging from hydrophilic to superhydrophobic. However, the maximum value of residence time for the non-Newtonian droplet is achieved when the stepwise pattern of hydrophilic to superhydrophobic is adopted.

**Keywords:** Droplet impact; hybrid surface; hydrophobicity; spreading factor; residence time.

**Nomenclature**

| | | | |
|---|---|---|---|
| $A$ | Cell area | $T$ | temperature |
| $Cou$ | Courant number | $V$ | Velocity vector |
| $D_0$ | Initial diameter of drop | $p$ | Pressure |
| $d$ | Droplet diameter | $Re$ | Reynolds number<br>$\mathrm{Re}=(\rho DV)/\mu$ |
| $\lvert e_{i1} \rvert$ | gradient function | $We$ | Weber number<br>$We=(\rho DV^2)/\sigma$ |
| $E$ | Total energy | *Greek letter* | |
| $f$ | advection function | $\sigma$ | Surface tension |
| $\bar{F}_b$ | volume force | $\tau$ | Shear stress |
| $g$ | gravity | $\rho$ | Density |
| $k_{eff}$ | effective thermal conductivity | $\eta$ | Viscosity |
| $S_h$ | volumetric heat sources | $\dot{\gamma}$ | Shear rate |
| $t$ | time | $\alpha$ | fluid's volume fraction |

## 1. Introduction

Droplet impact upon solid surfaces is an important phenomenon frequently occurs in natural and industrial applications (Abolghasemibizaki & Mohammadi, 2018; Khojasteh, Kazerooni, Salarian, & Kamali, 2016; Khojasteh, Kazerooni, & Marengo, 2019; Lin et al., 2018). The key factors influencing the post-impingement outcomes (e.g. spreading and bouncing) are droplet's size, impact velocity/angle, physical properties of the liquid, surface tension, and surface characteristics (e.g. wettability) (Bordbar, Taassob, Khojasteh, Marengo, & Kamali, 2018). Among these factors, surface wettability can be effectively applied to control the interactions between liquid drops and solid surfaces (Fernández et al., 2017; Gogolides, Ellinas, & Tserepi, 2015). To illustrate, superhydrophilic surfaces have both advancing and receding contact angles close to 0°, representing high surface energies. In contrast to these two contact angles, the static contact angle of superhydrophobic surfaces is larger than 150°. This highlights the low contact angle hysteresis and indicates that the difference between the advancing and receding contact angles is less than 10° (Akhtari & Karimi, 2020; Ueda & Levkin, 2013). The phenomenon of liquid droplets undergoing collision with solid surfaces with a constant contact angle has been examined extensively (Gelissen, van der Geld, Baltussen, & Kuerten, 2020; Rashidian, Sellier, & Mandin, 2019; Yeganehdoust, Attarzadeh, Karimfazli, & Dolatabadi, 2020). Yet, the process of droplet impact upon a single surface with a combination of various contact angles (known as hybrid surface) requires further attention. Gaining a deep insight into droplet impact on hybrid surfaces can provide new functionalities and possibilities in a wide range of applications such as biotechnological, biomolecular, microfluidic, encapsulation and electrochemical technologies (Diewald et al., 2020; Li, Yu, Zhou, & Yan, 2017; Shen, Liu, Wu, Yao, & Zhang, 2020; Šikalo, Tropea, & Ganić, 2005).

Modifying the wettability characteristics of a surface can control the movement and deflection of droplets (Nilsson & Rothstein, 2012), transport droplets without using external energy input (i.e. electric field) (Khojasteh et al., 2020) and avoid/promote formation of tiny satellite droplets (Mertaniemi et al., 2011). The methods for fabricating hydrophilic-superhydrophobic patterns were presented by Ueda and Levkin (Ueda & Levkin, 2013). They reported that these patterned surfaces can be employed to precisely control the geometry and shape of droplets after the impact; separate peptides of different wettabilities, manage bio-adhesion; form high-density cell microarrays; allow different substances or cell types to be isolated in each individual spot on the same substrate; and offset printing. Further, Song et al. (Song, Song, Hu, Du, & Zhou, 2015) experimentally tested droplet impact on a substrate where superhydrophobic patterns (contact angle of 165°) were fabricated on a hydrophilic glass slide (contact angle of 50°). They noted that the droplet can be split during the impact on the hybrid surface with a single stripe, and the split time is independent of the impact velocity and is smaller than the contact time when only a fully superhydrophobic surface is used. Li et al. (Li et al., 2017) analyzed the droplet migration on hydrophobic–hydrophilic hybrid surfaces textured with pillars, consisting of hydrophobic side walls and hydrophilic tops. They observed that the migration process gradually accelerated when the droplet covers more hydrophilic area.

Evidently, there exist several studies on understanding of the droplet impact upon solid surfaces with various contact angles. Yet, there is still a lack of examination regarding droplet impinging on the superhydrophobic-hydrophobic–hydrophilic hybrid surfaces. Therefore, this study aims to investigate the dynamics of Newtonian and non-Newtonian droplets impacting onto hybrid surfaces through three-dimensional numerical simulations. To this end, a finite volume method with the volume of fluid (VOF) model, adaptive grid technique, and variable time-step method in

Ansys-Fluent are employed. A wide variety of hybrid surfaces ranging from hydrophilic to hydrophobic to superhydrophobic or vice versa are considered to obtain detailed understanding of the process of droplet impact on these surfaces (i.e. Spreading diameter, droplet shape deformation, and velocity distribution within the droplet).

## 2. Problem configuration and numerical method

Figure 1a shows a schematic of the initial condition of the considered droplets with the characteristics presented in Table 1. The initial diameter of the droplet ($d_0$) is $227\times10^{-5}$ m and the Weber number is 32. Additionally, the initial pressure of the computational domain is kept constant at 1 atm. The current analysis assumes an incompressible laminar flow, and hence, the governing equations include conservation of mass, momentum, and energy in the following forms.

Continuity:

$$\nabla\cdot\bar{V}=0 \tag{1}$$

Momentum:

$$\frac{\partial\bar{V}}{\partial t}+\nabla\cdot\left(\bar{V}\bar{V}\right)=-\frac{1}{\rho}\nabla p+\frac{1}{\rho}\nabla\cdot\tilde{\tau}+\frac{1}{\rho}\bar{F}_b \tag{2}$$

Energy:

$$\frac{\partial}{\partial t}\left(\rho E\right)+\nabla\cdot\left(\bar{V}\left(\rho E+p\right)\right)=\nabla\cdot\left(k_{eff}\nabla T\right)+S_h \tag{3}$$

The volume force, $\bar{F}_b$, on the right-hand side of Eq. (2) represents the gravitational and the surface tension forces (Pasandideh-Fard, Pershin, Chandra, & Mostaghimi, 2002). The importance of surface tension effect is determined based on the value of Weber number. The volume of fluid (VOF) model treats energy, $E$, and temperature, $T$, as mass-averaged variables:

$$E=\frac{\sum_{q=1}^{n}\alpha_q\rho_q E_q}{\sum_{q=1}^{n}\alpha_q\rho_q} \tag{4}$$

where $E_q$ depends on the specific heat of each phase and the average temperature. Furthermore, fluid density and effective thermal conductivity ($k_{eff}$) vary among the phases. The source term, $S_h$, contains the volumetric heat sources.

The employed finite volume method has been used with the VOF approach to track the temporal evolution of the liquid free surface (Son & Kim, 2009). It is noted that the wide application of this approach has turned it into an approved method for predicting droplet impact (Bussmann, Mostaghimi, & Chandra, 1999; Yali, Lan, Shengqiang, & Guiying, 2014; Yokoi, Vadillo, Hinch, & Hutchings, 2009). A color function, *f*, is introduced to represent the volume fraction of the liquid phase in the computational cells (Baraldi, Dodd, & Ferrante, 2014). If the control volume is filled with a single liquid phase, the color function is set to one, while it is zero when the control volume is filled with pure air (Aniszewski, Ménard, & Marek, 2014; Karim, Prasad, & Rahman, 2014). Otherwise, the color function value lies between zero and one. The advection function (*f*) is expressed by the following equation.

$$\frac{\partial f}{\partial t} + \left(\vec{V} \cdot \nabla\right) f = 0 \tag{5}$$

In addition, a power law relationship between viscosity and shear rate is assumed to model non-Newtonian rheology. Here, the following power-law function is used (Taghizadeh & Razavi, 2009),

$$\eta = \underbrace{\exp\left[\alpha\left(1/\left(T - T_0\right) - 1/\left(T_\alpha - T_0\right)\right)\right]}_{Arrhenius\ law} k\dot{\gamma}^{n-1} \tag{6}$$

where, *k* and *n* are measures of the average fluid viscosity and the deviation of the fluid from the Newtonian behavior, respectively. The values of *k* and *n* and the additional properties of the shear-thinning non-Newtonian droplet properties are presented in Table 1. When the value of *n* is lower than one, the droplet is considered as the shear-thinning (pseudo-plastics) non-Newtonian fluid

named X0.1 (Moon, Kim, & Lee, 2014). Further, to reduce the numerical error and to improve convergence, the grid adaptation (Mousavi & Roohi, 2014) and adaptive time step (John & Rang, 2010) techniques were used. In this regard, the gradient approach to mesh adaptation was used in which the gradient function takes the following form:

$$\left|e_{i1}\right| = \left(A_{cell}\right)^{\frac{r}{2}} \left|\nabla f\right| . \tag{7}$$

In this method, the global time step based on courant number is calculated as follows.

$$\Delta t_{global} = \frac{Cou_{global}}{\max\left(\sum \frac{outgoing\ flux}{volume}\right)_{each\ cell}} \tag{8}$$

It should be noted that since the simulation of the droplet process is sensitive to the Courant number, the variable time stepping method was employed to keep the Courant number at or below 0.1.

It is emphasized that in this study, wettability is characterized by an equilibrium contact angle model. It has been demonstrated that this model presents a good agreement between the numerical simulations and experiments (Bordbar et al., 2018; Marengo, Antonini, Roisman, & Tropea, 2011).

**3. Grid independency and validation**

To check the grid independency, three grids with 35000, 65000, and 150000 cells were tested, and the results of the maximum spreading diameter were presented in Table 2. Clearly, the results do not change for grids containing more than 65000 cells. Further, Fig. 1b demonstrates a comparison between the computed dimensionless diameter using 65000 cells with the experimental data reported by Moon et al. (Moon et al., 2014). The obtained results from the present numerical method are consistent with the experimental data for shear-thinning non-Newtonian droplet. In addition, Fig. 1c displays a comparison between the numerical dynamic contact history images

and experimental data (Moon et al., 2014) for various impact time. From Figs. 1b-c, it is concluded that the VOF model with considering the equilibrium contact angle can accurately predict the droplet spreading and receding behaviors during impact with the solid surface.

## 4. Results and Discussion

In this section, the dynamic behavior of a Newtonian droplet in collision with two surfaces with contact angles of 80° (hydrophilic surface – named pattern-1 (P1)) and 160° (superhydrophobic surface – named pattern-2 (P2)) were investigated. Fig. 2 shows the dependency of the droplet spreading factor ($SF=d/D_0$) on the surface contact angle. Evidently, changing the surface wettability from hydrophilic to superhydrophobic led to variations in droplet structure. This means that contact angle plays an important role in spreading and retraction times, maximum spreading factor, and the time of maximum spreading (residence time). Increasing contact angle also reduces the hydrophilic force and therefore, the droplet does not tend to spread over the surface. As a consequent, superhydrophobic surface exhibits a smaller droplet spreading factor in comparison to a hydrophilic surface.

### 4.1 Effects of hybrid surfaces

In this section, the effects of implementing different hydrophilic-hydrophobic-superhydrophobic hybrid surfaces with various wettabilities were investigated. To serve this purpose, Figs. 3&4 show that the surface wettability varies with linear and stepwise patterns including hydrophilic-hydrophobic-superhydrophobic hybrid surfaces as patterns P3 and P5 as well as superhydrophobic-hydrophobic-hydrophilic hybrid surfaces as patterns P4 and P6, respectively. The boundary and initial conditions of the evaluated cases are similar to those presented in Table 1, and four different functions describing patterns P3 to P6 (see Fig. 4) were used to change the surface contact angle (C.A.).

Figure 5a-b represents the SF of Newtonian droplet impacting onto the surfaces with patterns of P3-P4 and P5-P6. It can be seen that when P3 and P5 patterns are considered, the maximum SF is larger than those of P4 and P6 patterns. Due to the existence of hydrophilic force on hybrid surfaces, the drop tends to move from the hydrophobic sections to the hydrophilic part and the migration process gradually speeds up. From another perspective, using hydrophilic to hydrophobic surface can increase the contact length between the droplet and the surface with a reduction in the hydrophobicity of the surface. Finally, the amount of the SF for patterns of P3 and P5 is more than patterns of P4 and P6. By comparing the P3 and P5 patterns, more wetted area is observable for the linear pattern of changing wettability (P3). Considering distribution of the contact angles on the surfaces in these three patterns, the droplet is permanently affected by the hydrophilic force in P3, and this force increases linearly with the drop motion. This is mainly attributed to the fact that the enhancement of the energy barrier of P5 is more than that of P3, which leads to a decrease in the hydrophilic force. Therefore, the droplet tends to spread more quickly in P3. Eventually, the amount of SF in P3 is more than in P5. As stated earlier, the presence of a hydrophilic-hydrophobic-superhydrophobic hybrid surface (P3 and P5) increases the amount of SF. The reason for the increase in the SF level is the presence of hydrophilic force which increases the pulling force of the droplet and thus enhances the spreading process.

Figure 6 compares the maximum SF as well as the residence time (RT) (Yong Park, Min, Granick, & Cahill, 2012) of the Newtonian droplet in collision with the mentioned patterns. Evidently, maximum SF of P3 is higher than that of in P1 as homogeneous hydrophilic surface. In addition, when a linear pattern is used, the spreading drop can cover approximately 65% of the surface, but it covers 59% of the surface for a stepwise pattern. The highest RT of the droplet is obtained when colliding with P3 pattern. A remarkable feature is that the larger SP can lead to longer RT. This

means that the RT of P3 pattern is 68.75% more than the RT of P5 pattern and also this value has increased by 18.75% for P3 in comparison with P1. Further, for P1, P3, and P5, the edge of the drop sticks to the surface due to the presence of hydrophilic force, but for P2, P4, and P6, the edge of the drop tends to separate from the surface. Therefore, the droplet receding time in P2, P4, and P6 patterns is less than that of in P1, P3, and P5.

In general, due to the changes in RT values for different patterns, the contents of this section can be used as a passive control method in different applications. For example, to improve the heat transfer process, which is directly related to RT, the surface with P3 pattern can be used. Conversely, heat transfer can be reduced by using a surface with P6 pattern. Figure 7 shows the shape of the droplet at different times for two patterns of P3 and P6 as the patterns with the highest and lowest spread factors. According to this figure, the drop spreads faster on the surface with P6 pattern because it is less affected by adhesion and the receding process for this pattern begins in less time. Considering the behavior of the droplet in contact with a surface with P3 pattern, the droplet requires more time to reach its maximum spreading on the surface. Also, by comparing the droplet deformation, the entire area of the droplet tends to stick to the surface when using P3. However, when the droplet collides with the surface with P6 pattern, the edge of the droplet is detached from the surface due to the effect of the hydrophobic force, and this state is also seen when reaching the maximum wetted surface.

Overall, the results of this section shows that the droplet spreading behavior strongly depends on the surface wettability distribution. For instance, for a stepwise pattern, it depends on the number of steps so that for cases with higher steps the spreading behavior is similar to the cases with linear patterns (i.e., P5 and P6). As such, surface characteristics primarily govern the droplet dynamics.

**4.2 Non-Newtonian droplet impact**

In this section, the behavior of non-Newtonian droplets on a surface with varying contact angles and with the properties in Table 1 were examined. Figures 8a-c displays the SF when a non-Newtonian droplet collides with the surface with P1-P2, P3-P4, and P5-P6 patterns. Furthermore, Figure 9 compares maximum SF and RT for non-Newtonian droplets when using P1-P6 patterns. Evidently, the highest and lowest SFs belong to the surfaces with P3 and P6 patterns, respectively. As shown in Fig. 8, the longest time to reach the maximum SF for a non-Newtonian droplet is obtained when using surface with P5 pattern, while in the Newtonian drop this value belongs to a surface with P3 pattern. The reason for this change in behavior is the difference in the viscosity of the non-Newtonian drop which is related to shear rate and 9-60 times larger than the viscosity of Newtonian droplet. Also, compared to Newtonian droplets, the maximum SF for all similar patterns has decreased. This is because for the non-Newtonian droplet the viscosity is larger than that of the Newtonian droplet and therefore, the contribution of viscous forces increases. Consequently, it creates a resistance to the movement of the droplet on the surface. In addition, it is clear from Fig. 9 that the maximum and minimum RTs are obtained when the surfaces with P5 and P6 patterns were used, respectively. Furthermore, the spreading drop can cover approximately 58% of the surface with linear pattern (P3) and this value is 49% for the surface with the stepwise pattern (P5). Comparison between RT for Newtonian and non-Newtonian droplet shows that the maximum RT is related to maximum SF for Newtonian droplets, while it is not the case for non-Newtonian droplets where the maximum RT occurs for P5 that does not exhibit the largest SF.

Figures 10 and 11 show a comparison between the Newtonian and the non-Newtonian droplet structures and wall shear stress distributions at various impact times, respectively. In both cases, the droplet edge is attached to the surface (see Fig. 10). However, the maximum wetted surface of Newtonian droplet is 10.87% more than that of the non-Newtonian one due to the fact that the non-

Newtonian droplets are more viscous than the Newtonian ones. Therefore, the resistant force against the spreading of the non-Newtonian droplet is larger in comparison to the Newtonian droplet. Figure 11 illustrates the wall shear stress as a main factor of resistance against the fluid motion. There are different behaviors in shear stress distributions at the edge of the Newtonian and non-Newtonian droplets. This is such that the value of this parameter for non-Newtonian droplet is much more than (5 to 15 times related to impact time) that of the Newtonian one at the edge of the droplet. As a result, the SF of Newtonian droplet is more than one for the non-Newtonian droplet.

Figure 12 represents the velocity distribution on the phase interfaces iso-surface with the value of 0.5 at the dimensionless time of 0.32, 0.7, 0.93, 1.18, and 1.26 for P5 and P6 patterns. Considering the behavior of droplets at the time steps of 1.18 and 1.26, while droplet is spreading on the surface with P5, the retraction of droplet on the surface with P6 is initiated. This is because hydrophilic surface plays a central role in P5 at these time, while for P6 the superhydrophobic surface has a leading role. In addition, the droplet migration can be promoted by increasing the role of contrast in surface wettability (hydrophobic or superhydrophobic surfaces) as illustrated in Fig. 12. The SF with P6 reaches its maximum value in a shorter time (approximately 0.62); consequently, the receding process occurs faster in the surface with P6. The above set of results highlight the ability of hybrid surfaces to manipulate the movement and deflection of droplets as well as transport droplets and control the bouncing behavior. These are of significance in industrial, biotechnological, bio-molecular, microfluidic, encapsulation and electrochemical applications.

## 5. Conclusions

While modifying the wettability characteristics of a surface can control the structure, movement, and deflection of droplets with numerous technological and industrial applications, studies

regarding droplet impacts onto a surface with a combination of various contact angles (known as hybrid surfaces) are scarce. To partially fill this knowledge gap, this study presents a numerical investigation on the dynamics of Newtonian and non-Newtonian droplets colliding with hybrid surfaces with various wettabilities. The results demonstrated that the amount of SF for patterns P1, P3 and P5 is more than that of patterns P2, P4, and P6 for both Newtonian and non-Newtonian droplets. The largest RT of the droplet is obtained when colliding with P3 pattern. Furthermore, for P1, P3, and P5, the edge of the drop sticks to the surface due to the presence of hydrophilicity force, but for P2, P4, and P6, the edge of the drop tends to separate from the surface. Therefore, the droplet receding time in P2, P4, and P6 patterns is much less than that when using P1, P3, and P5. In addition, the longest time to reach the maximum SF for a non-Newtonian droplet is obtained when using a surface with P5 pattern, while for the Newtonian drop this value belongs to the surface with P3 pattern. Moreover, the maximum and minimum RTs of non-Newtonian droplet are obtained when surfaces with P5 and P6 patterns are used, respectively, while for the Newtonian droplet the maximum RT is related to P3 pattern. Finally, the value of wall shear stress for non-Newtonian droplet is much more than that of Newtonian one at the edge of the droplets. These findings highlight the functionalities of hybrid surfaces in manipulating the spreading, retraction, contact time, and contact line of impacting droplet which have major applications in chemical, medical, and biotechnological industries, and thereby, requiring further attention.

**References**

Abolghasemibizaki, M., & Mohammadi, R. (2018). Droplet impact on superhydrophobic surfaces fully decorated with cylindrical macrotextures. *Journal of Colloid and Interface Science, 509*, 422-431. doi:https://doi.org/10.1016/j.jcis.2017.09.030

Akhtari, M. R., & Karimi, N. (2020). Thermohydraulic analysis of a microchannel with varying superhydrophobic roughness. *Applied Thermal Engineering, 172*, 115147. doi:https://doi.org/10.1016/j.applthermaleng.2020.115147

Aniszewski, W., Ménard, T., & Marek, M. (2014). Volume of Fluid (VOF) type advection methods in two-phase flow: A comparative study. *Computers & Fluids, 97*, 52-73. doi:https://doi.org/10.1016/j.compfluid.2014.03.027

Baraldi, A., Dodd, M. S., & Ferrante, A. (2014). A mass-conserving volume-of-fluid method: Volume tracking and droplet surface-tension in incompressible isotropic turbulence. *Computers & Fluids, 96*, 322-337. doi:https://doi.org/10.1016/j.compfluid.2013.12.018

Bordbar, A., Taassob, A., Khojasteh, D., Marengo, M., & Kamali, R. (2018). Maximum Spreading and Rebound of a Droplet Impacting onto a Spherical Surface at Low Weber Numbers. *Langmuir, 34*(17), 5149-5158. doi:10.1021/acs.langmuir.8b00625

Bussmann, M., Mostaghimi, J., & Chandra, S. (1999). On a three-dimensional volume tracking model of droplet impact. *Physics of Fluids, 11*(6), 1406-1417. doi:10.1063/1.870005

Diewald, F., Lautenschlaeger, M. P., Stephan, S., Langenbach, K., Kuhn, C., Seckler, S., . . . Müller, R. (2020). Molecular dynamics and phase field simulations of droplets on surfaces with wettability gradient. *Computer Methods in Applied Mechanics and Engineering, 361*, 112773. doi:https://doi.org/10.1016/j.cma.2019.112773

Fernández, A., Francone, A., Thamdrup, L. H., Johansson, A., Bilenberg, B., Nielsen, T., . . . Kehagias, N. (2017). Design of Hierarchical Surfaces for Tuning Wetting Characteristics. *ACS Applied Materials & Interfaces, 9*(8), 7701-7709. doi:10.1021/acsami.6b13615

Gelissen, E. J., van der Geld, C. W. M., Baltussen, M. W., & Kuerten, J. G. M. (2020). Modeling of droplet impact on a heated solid surface with a diffuse interface model. *International Journal of Multiphase Flow, 123*, 103173. doi:https://doi.org/10.1016/j.ijmultiphaseflow.2019.103173

Gogolides, E., Ellinas, K., & Tserepi, A. (2015). Hierarchical micro and nano structured, hydrophilic, superhydrophobic and superoleophobic surfaces incorporated in microfluidics, microarrays and lab on chip microsystems. *Microelectronic Engineering, 132*, 135-155. doi:https://doi.org/10.1016/j.mee.2014.10.002

John, V., & Rang, J. (2010). Adaptive time step control for the incompressible Navier–Stokes equations. *Computer Methods in Applied Mechanics and Engineering, 199*(9), 514-524. doi:https://doi.org/10.1016/j.cma.2009.10.005

Karim, M. M., Prasad, B., & Rahman, N. (2014). Numerical simulation of free surface water wave for the flow around NACA 0015 hydrofoil using the volume of fluid (VOF) method. *Ocean Engineering, 78*, 89-94. doi:https://doi.org/10.1016/j.oceaneng.2013.12.013

Khojasteh, D., Kazerooni, M., Salarian, S., & Kamali, R. (2016). Droplet impact on superhydrophobic surfaces: A review of recent developments. *Journal of Industrial and Engineering Chemistry, 42*, 1-14. doi:https://doi.org/10.1016/j.jiec.2016.07.027

Khojasteh, D., Kazerooni, N. M., & Marengo, M. (2019). A review of liquid droplet impacting onto solid spherical particles: A physical pathway to encapsulation mechanisms. *Journal of Industrial and Engineering Chemistry, 71*, 50-64. doi:https://doi.org/10.1016/j.jiec.2018.11.030

Khojasteh, D., Manshadi, M. K. D., Mousavi, S. M., Sotoudeh, F., Kamali, R., & Bordbar, A. (2020). Electrically modulated droplet impingement onto hydrophilic and (super)hydrophobic solid surfaces. *Journal of the Brazilian Society of Mechanical Sciences and Engineering, 42*(4), 153. doi:10.1007/s40430-020-2241-6

Li, Q., Yu, Y., Zhou, P., & Yan, H. J. (2017). Droplet migration on hydrophobic–hydrophilic hybrid surfaces: a lattice Boltzmann study. *RSC advances, 7*(24), 14701-14708. doi:10.1039/C6RA28665H

Lin, S., Zhao, B., Zou, S., Guo, J., Wei, Z., & Chen, L. (2018). Impact of viscous droplets on different wettable surfaces: Impact phenomena, the maximum spreading factor, spreading time and post-impact oscillation. *Journal of Colloid and Interface Science, 516*, 86-97. doi:https://doi.org/10.1016/j.jcis.2017.12.086

Marengo, M., Antonini, C., Roisman, I. V., & Tropea, C. (2011). Drop collisions with simple and complex surfaces. *Current Opinion in Colloid & Interface Science, 16*(4), 292-302. doi:https://doi.org/10.1016/j.cocis.2011.06.009

Mertaniemi, H., Jokinen, V., Sainiemi, L., Franssila, S., Marmur, A., Ikkala, O., & Ras, R. H. A. (2011). Superhydrophobic Tracks for Low-Friction, Guided Transport of Water Droplets. *Advanced Materials, 23*(26), 2911-2914. doi:10.1002/adma.201100461

Moon, J. H., Kim, D. Y., & Lee, S. H. (2014). Spreading and receding characteristics of a non-Newtonian droplet impinging on a heated surface. *Experimental Thermal and Fluid Science, 57*, 94-101. doi:https://doi.org/10.1016/j.expthermflusci.2014.04.003

Mousavi, S. M., & Roohi, E. (2014). Three dimensional investigation of the shock train structure in a convergent–divergent nozzle. *Acta Astronautica, 105*(1), 117-127. doi:https://doi.org/10.1016/j.actaastro.2014.09.002

Nilsson, M. A., & Rothstein, J. P. (2012). Using sharp transitions in contact angle hysteresis to move, deflect, and sort droplets on a superhydrophobic surface. *Physics of Fluids, 24*(6), 062001. doi:10.1063/1.4723866

Pasandideh-Fard, M., Pershin, V., Chandra, S., & Mostaghimi, J. (2002). Splat shapes in a thermal spray coating process: Simulations and experiments. *Journal of Thermal Spray Technology, 11*(2), 206-217. doi:10.1361/105996302770348862

Rashidian, H., Sellier, M., & Mandin, P. (2019). Dynamic wetting of an occlusion after droplet impact. *International Journal of Multiphase Flow, 111*, 264-271. doi:https://doi.org/10.1016/j.ijmultiphaseflow.2018.12.002

Shen, C., Liu, L., Wu, S., Yao, F., & Zhang, C. (2020). Lattice Boltzmann simulation of droplet condensation on a surface with wettability gradient. *Proceedings of the Institution of Mechanical Engineers, Part C: Journal of Mechanical Engineering Science*, 0954406219898220. doi:10.1177/0954406219898220

Šikalo, Š., Tropea, C., & Ganić, E. N. (2005). Impact of droplets onto inclined surfaces. *Journal of Colloid and Interface Science, 286*(2), 661-669. doi:https://doi.org/10.1016/j.jcis.2005.01.050

Son, Y., & Kim, C. (2009). Spreading of inkjet droplet of non-Newtonian fluid on solid surface with controlled contact angle at low Weber and Reynolds numbers. *Journal of Non-Newtonian Fluid Mechanics, 162*(1), 78-87. doi:https://doi.org/10.1016/j.jnnfm.2009.05.009

Song, D., Song, B., Hu, H., Du, X., & Zhou, F. (2015). Selectively splitting a droplet using superhydrophobic stripes on hydrophilic surfaces. *Physical Chemistry Chemical Physics, 17*(21), 13800-13803. doi:10.1039/C5CP01530H

Taghizadeh, M., & Razavi, S. M. A. (2009). Modeling Time-Independent Rheological Behavior of Pistachio Butter. *International Journal of Food Properties, 12*(2), 331-340. doi:10.1080/10942910701772048

Ueda, E., & Levkin, P. A. (2013). Emerging Applications of Superhydrophilic-Superhydrophobic Micropatterns. *Advanced Materials, 25*(9), 1234-1247. doi:10.1002/adma.201204120

Yali, G., Lan, W., Shengqiang, S., & Guiying, C. (2014). Simulation of dynamic characteristics of droplet impact on liquid film. *International Journal of Low-Carbon Technologies, 9*(2), 150-156. doi:10.1093/ijlct/ctu019

Yeganehdoust, F., Attarzadeh, R., Karimfazli, I., & Dolatabadi, A. (2020). A numerical analysis of air entrapment during droplet impact on an immiscible liquid film. *International Journal of Multiphase Flow, 124*, 103175. doi:https://doi.org/10.1016/j.ijmultiphaseflow.2019.103175

Yokoi, K., Vadillo, D., Hinch, J., & Hutchings, I. (2009). Numerical studies of the influence of the dynamic contact angle on a droplet impacting on a dry surface. *Physics of Fluids, 21*(7), 072102. doi:10.1063/1.3158468

Yong Park, J., Min, C.-K., Granick, S., & Cahill, D. G. (2012). Residence Time and Heat Transfer When Water Droplets Hit a Scalding Surface. *Journal of heat transfer, 134*(10). doi:10.1115/1.4006802

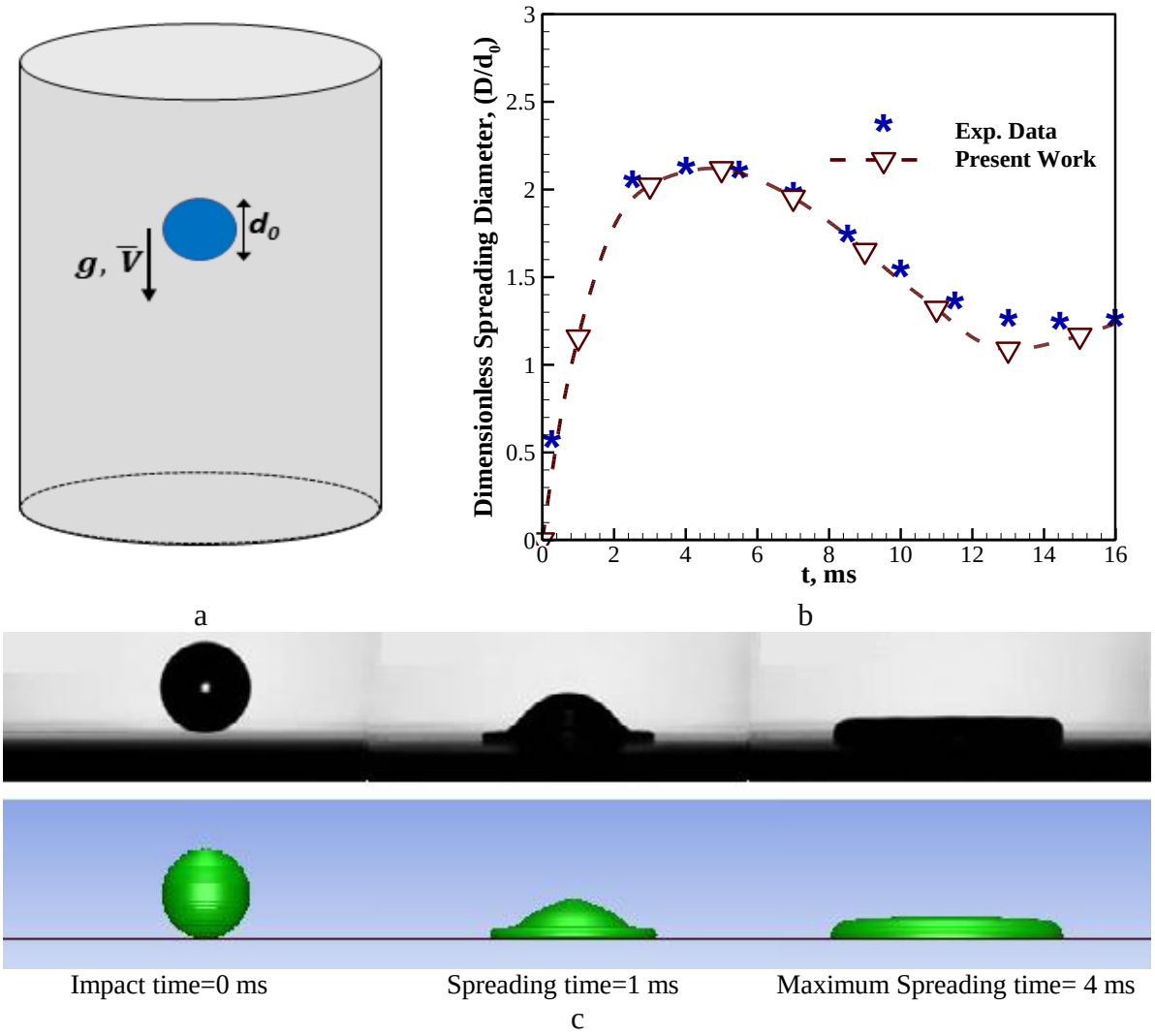


Fig. 1. a- A schematic of droplet impact initial condition and b&c Validation of the present finite volume code against the experimental data of Ref. (Moon et al., 2014).

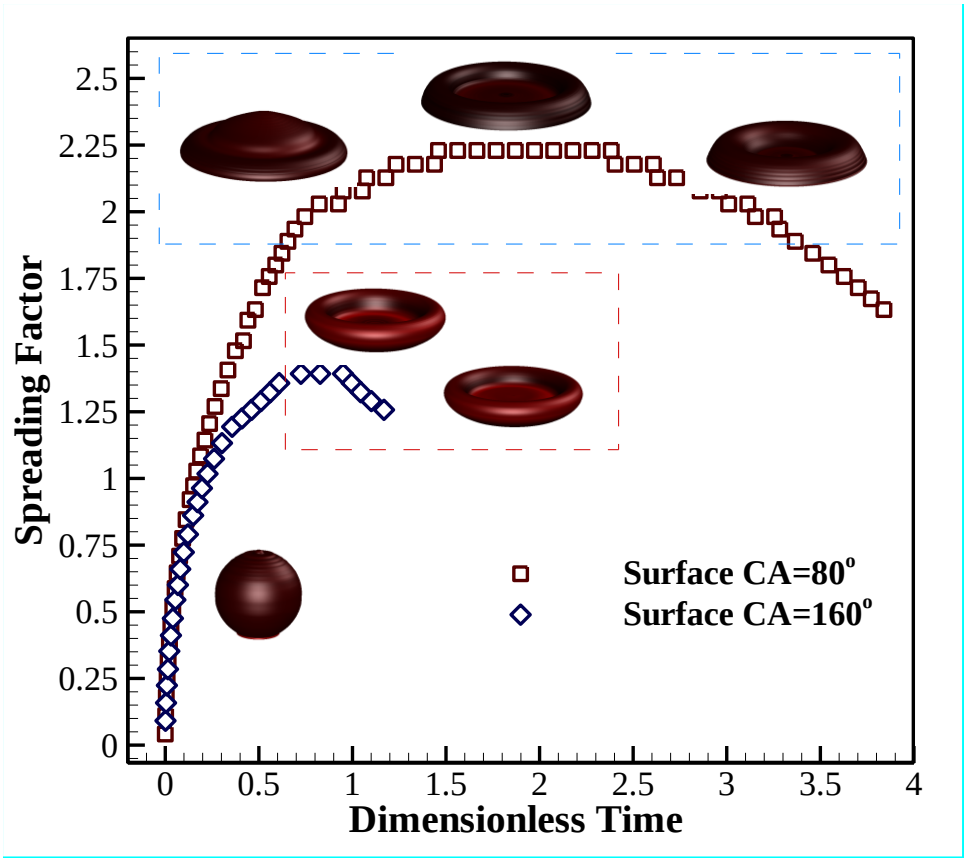


Fig. 2. SF of the Newtonian droplet in collision with hydrophilic and supoerhydrophobic surfaces

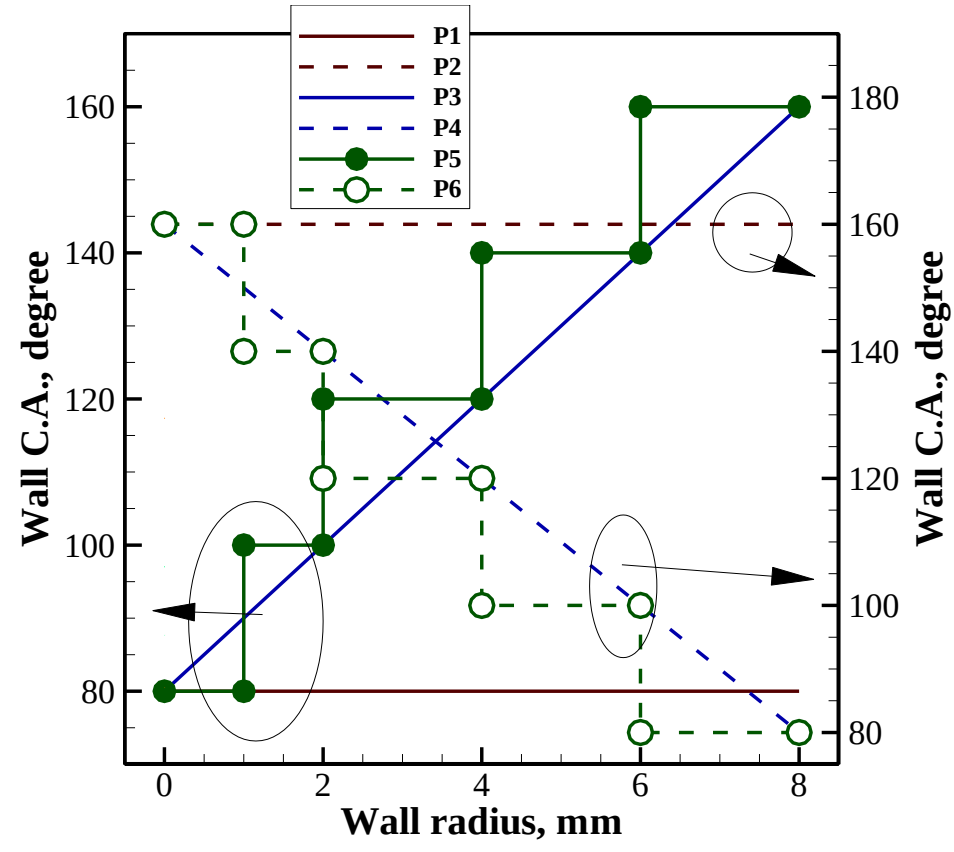


Fig. 3. Contact angle patterns for the wall

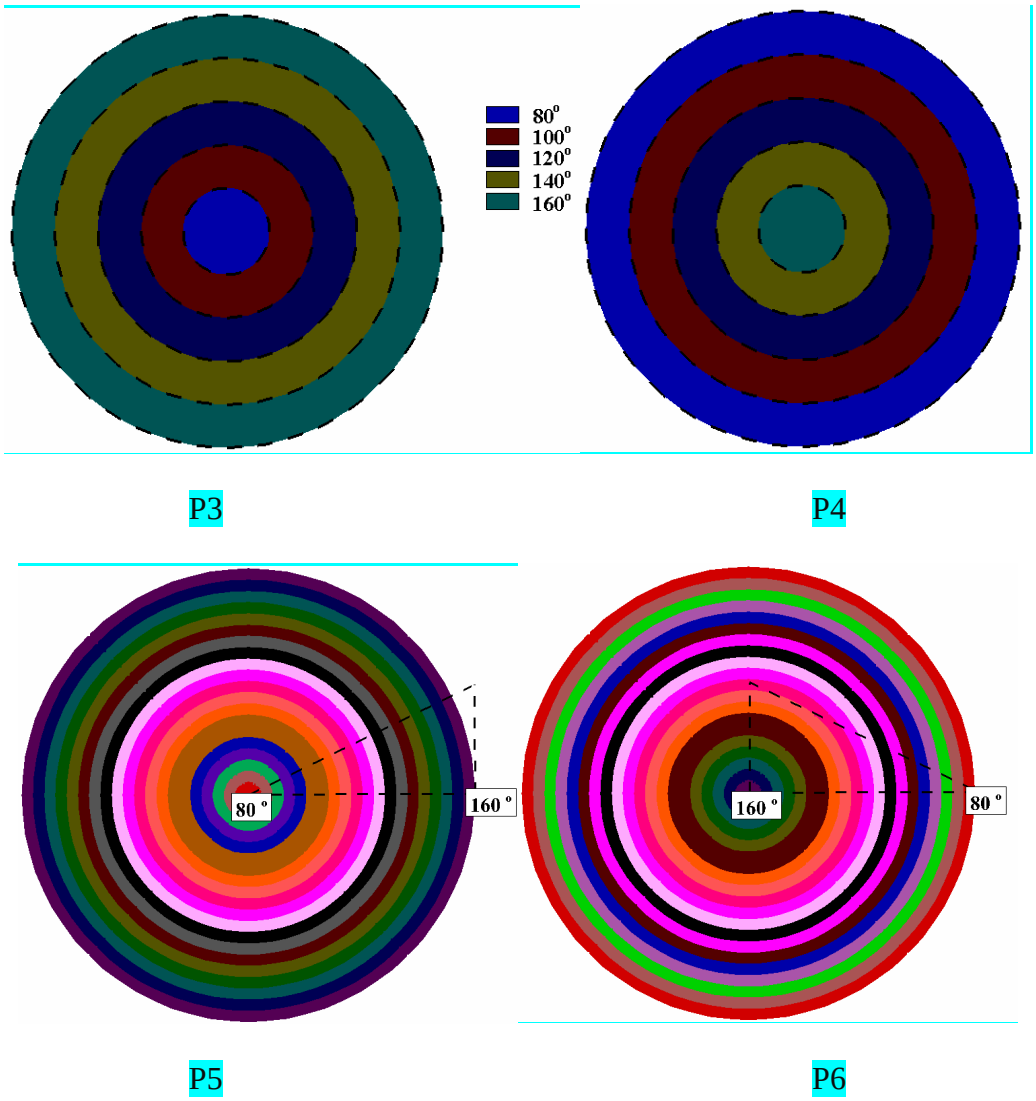


Fig. 4. Changes of contact angles for hybrid surfaces

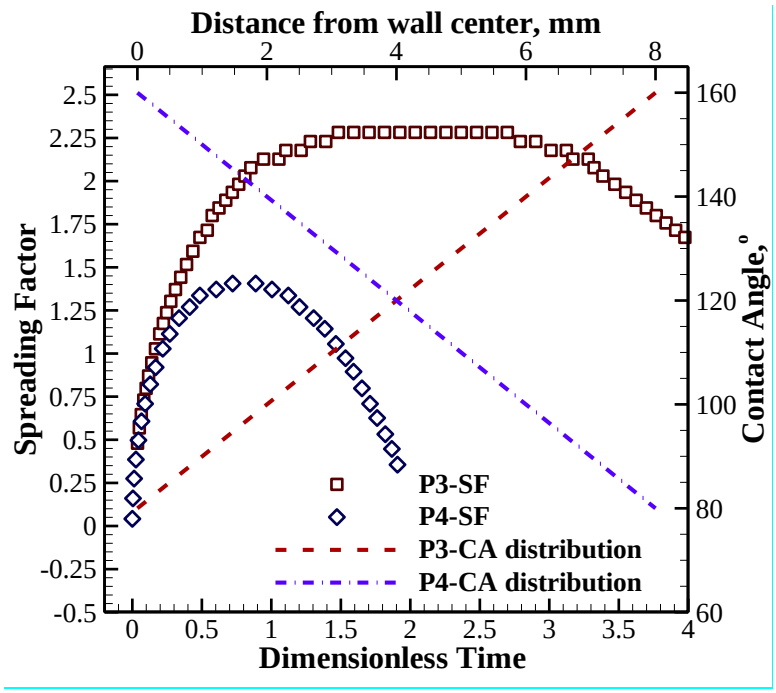


a

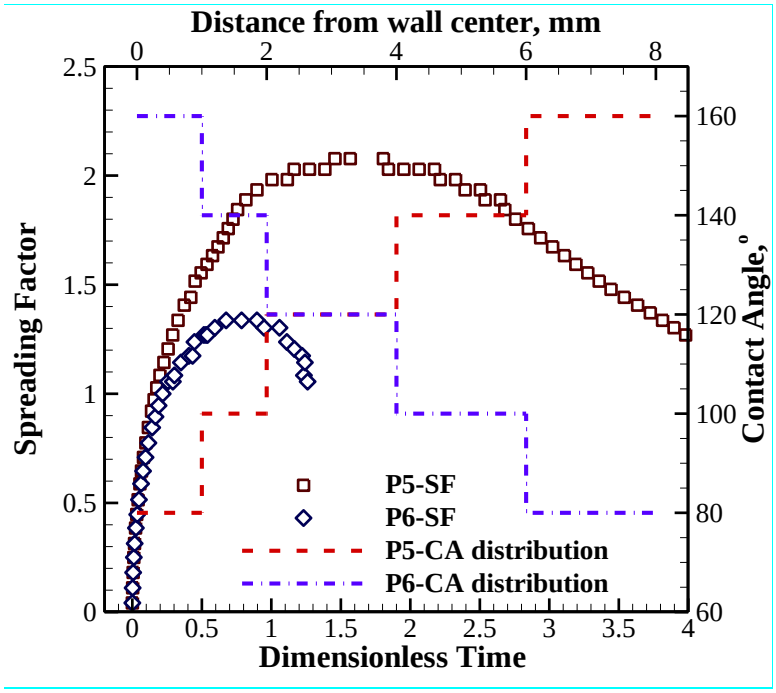


b

Fig. 5. SF of the Newtonian droplet with a- linear (P3-P4) and b- stepwise (P5-P6) contact angle patterns

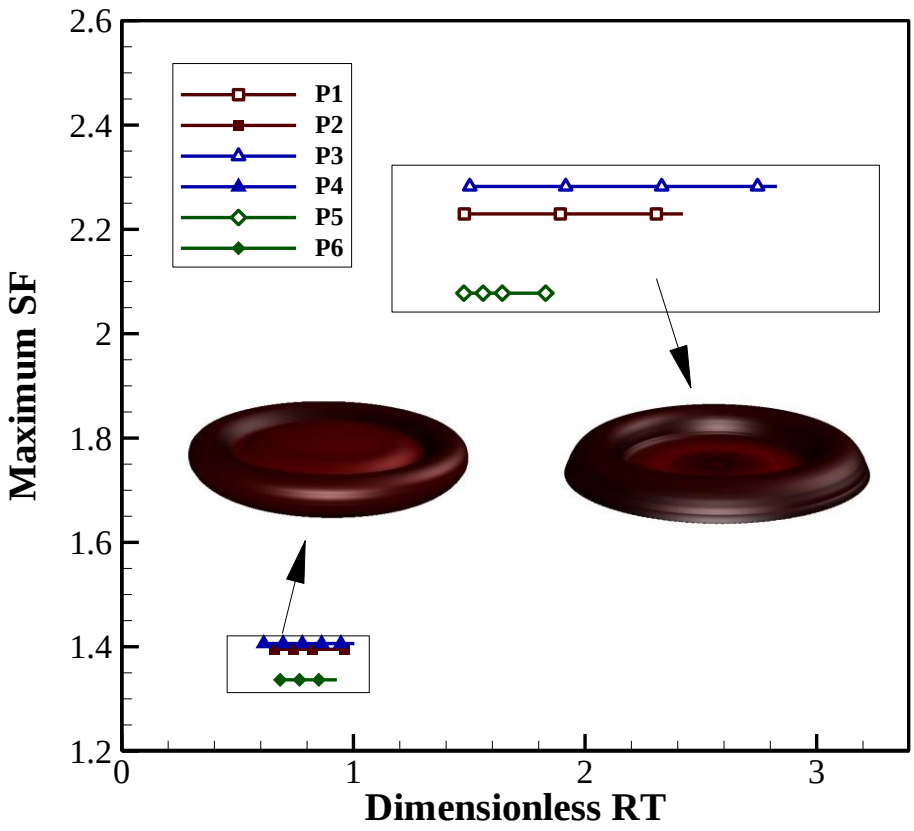


Fig. 6. Residence time of the Newtonian droplet impact

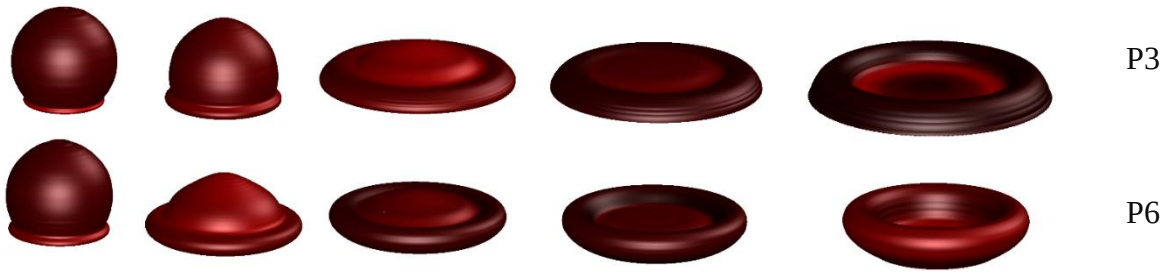


Fig. 7. Newtonian droplet structure during the impact time

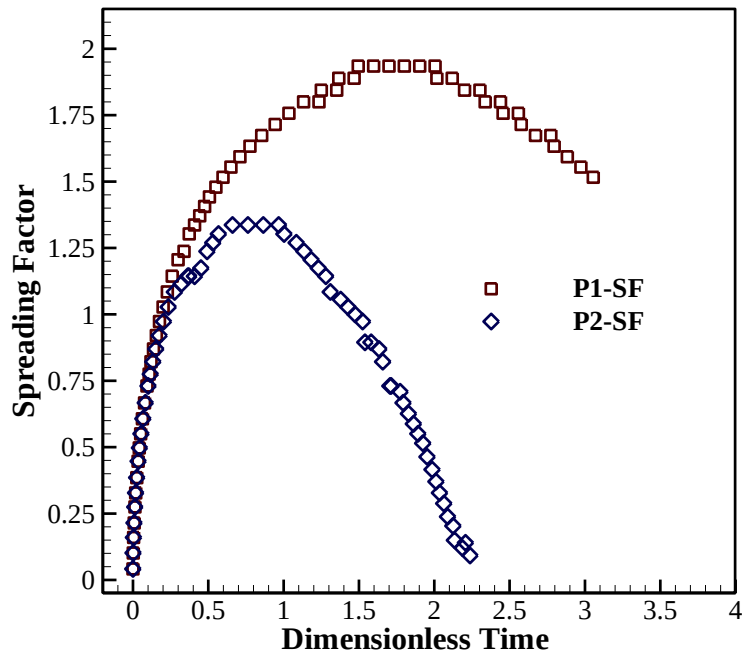


a

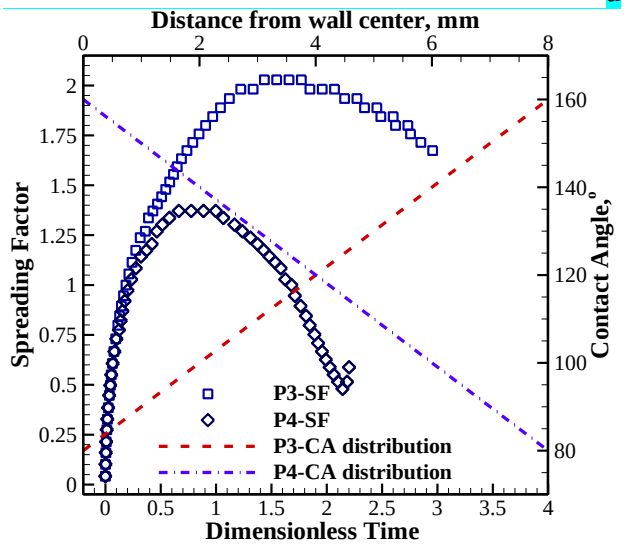


b

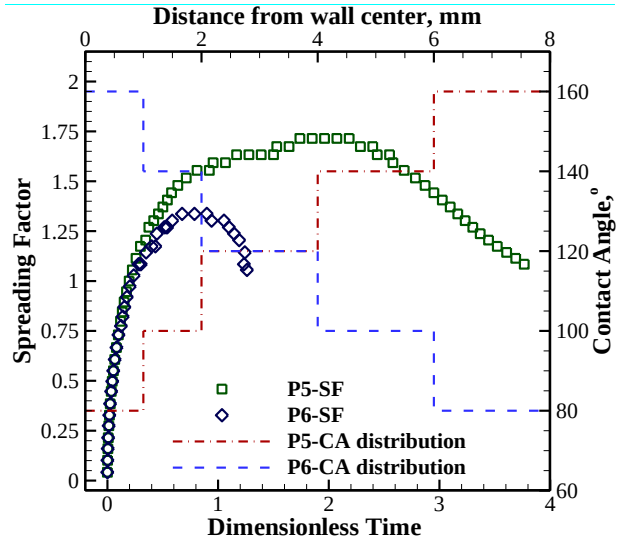


c

Fig. 8. Maximum SF for the non-Newtonian droplet in collision with a- constant (P1-P2), b- linear (P3-P4), and c- stepwise (P5-P6) contact angle patterns

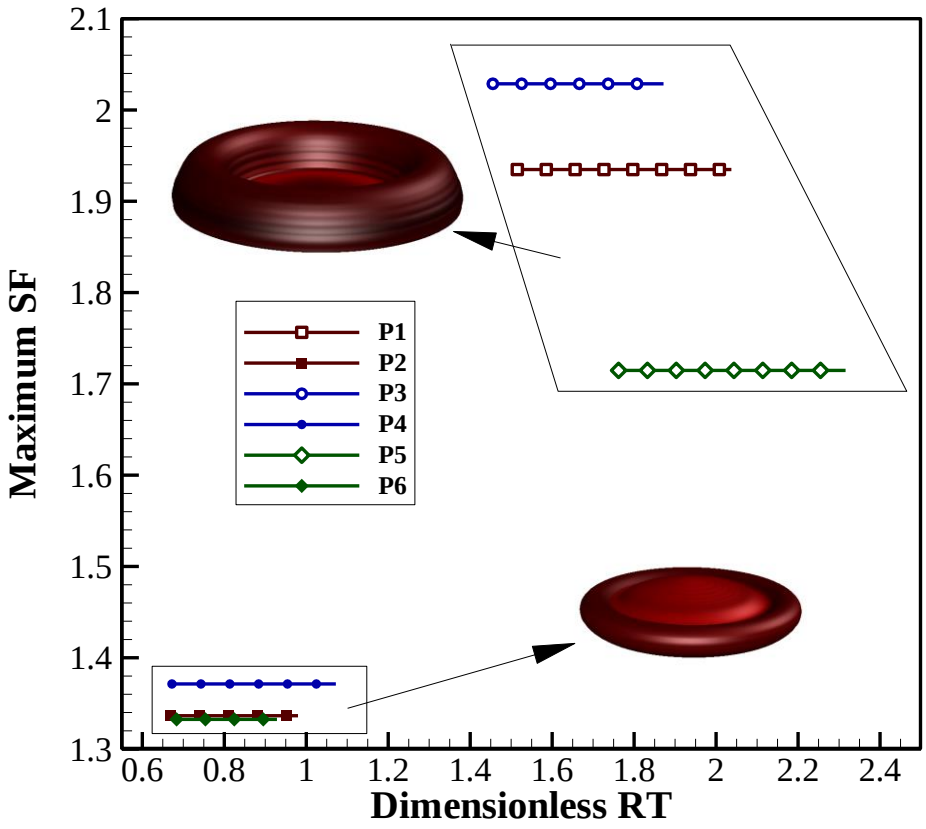


Fig. 9. Residence time of the non-Newtonian droplet

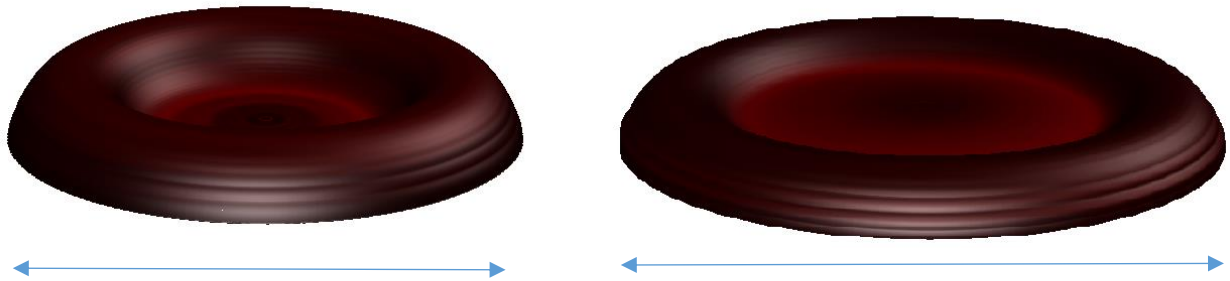

2.077 2.33

Non-Newtonian Newtonian

Fig. 10. Comparison between the structure of the Newtonian and non-Newtonian droplets at the time of maximum SF.

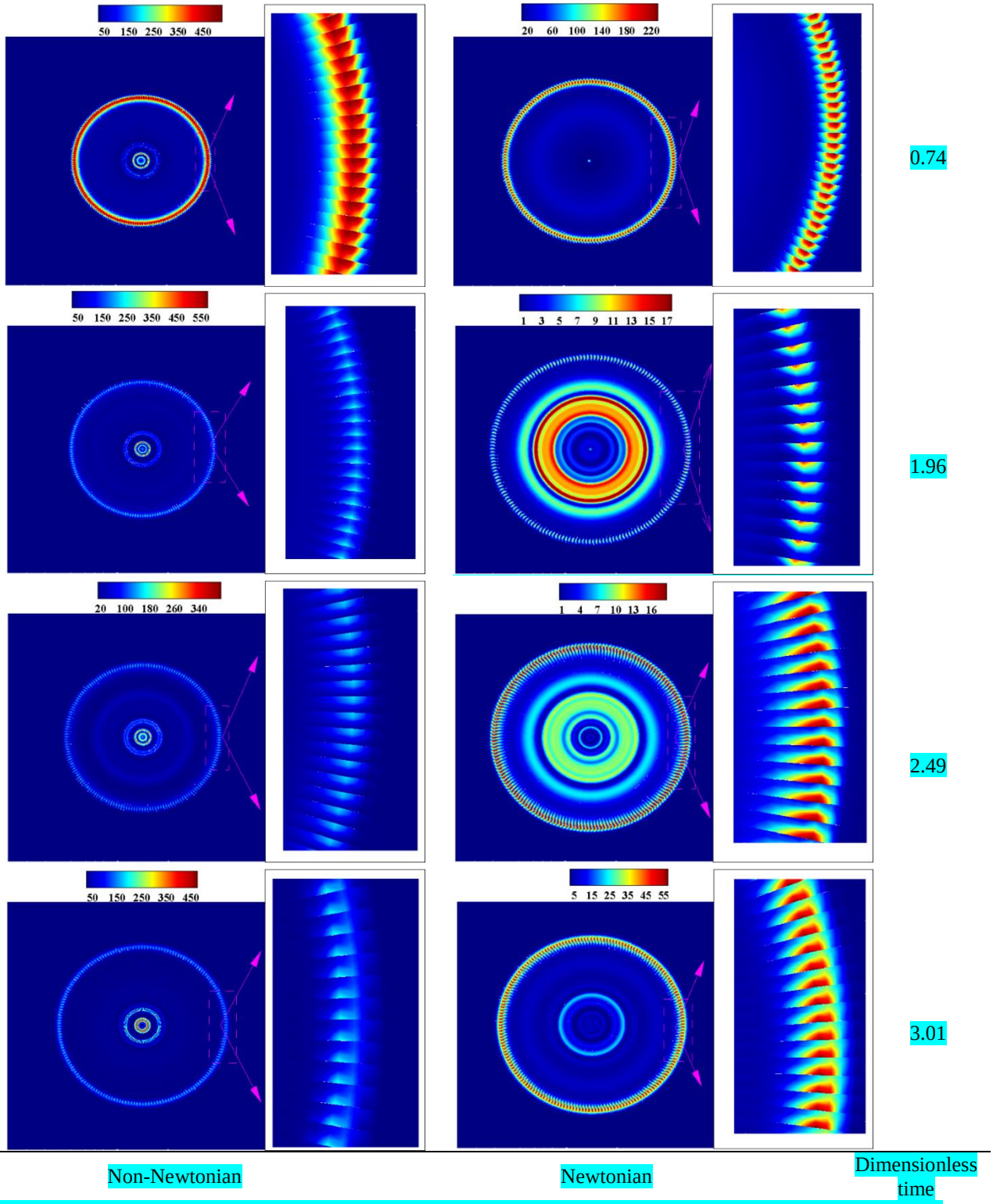


Fig.11. Wall shear stress (Pa) distribution of the Newtonian and the non-Newtonian droplets at the time of maximum SF.

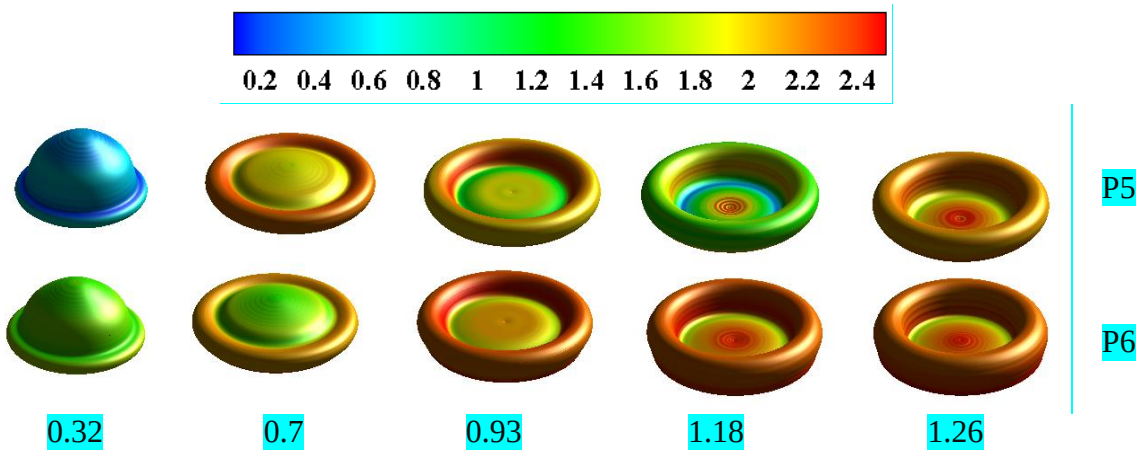


Figure 12. Velocity (m/s) distributions for droplet impact on surfaces with P5 and P6 patterns.

Table 1. Properties of DI-water and X0.1 droplets at 298.15 K, and initial condition of the droplet impact, consistent with Moon et al. (Moon et al., 2014).

| | $\mu_0$ (Pa.s) | P (kg/m$^3$) | n | K (Pa.s$^n$) | $\gamma_{LV}$ (N/m) | $\theta_e$ (◦) | $D_0$, (m) | Weber numbe |
|---|---|---|---|---|---|---|---|---|
| DI-water | 0.001 | 998.2 | - | - | 0.072 | 79.7 | $227\times10^{-5}$ | 32 |
| X0.1 | 0.375 | 999 | 0.41 | 0.1069 | 0.0707 | 79.7 | $227\times10^{-5}$ | 32 |

Table 2. Grid independency test

| Number of cells | 35000 | 65000 | 150000 |
|---|---|---|---|
| Maximum spreading diameter, | 2.7 | 2.1 | 2.11 |